




## Article

# The Effect of Metal Ratio and Precipitation Agent on Highly Active Iron-Manganese Mixed Metal Oxide Catalysts for Propane Total Oxidation

Parag M. Shah, Liam A. Bailey , David J. Morgan  and Stuart H. Taylor \* 

Cardiff Catalysis Institute, School of Chemistry, Cardiff University, Translational Research Hub, Maindy Road, Cardiff CF24 4HQ, UK; parag.manojshah@matthey.com (P.M.S.); bailey1a2@cardiff.ac.uk (L.A.B.); morgandj3@cardiff.ac.uk (D.J.M.)

\* Correspondence: taylorsh@cardiff.ac.uk

**Abstract:** Iron-manganese mixed metal oxide catalysts with a range of Fe:Mn ratios were synthesised by co-precipitation using sodium carbonate and evaluated for total propane oxidation. The  $\text{Fe}_{0.50}\text{Mn}_{0.50}\text{O}_x$  catalyst was the most active, and this was due to increased surface area along with the formation of a  $\text{Mn}_2\text{O}_3$  phase that was not present in the other catalysts. The effect of the precipitating agent was evaluated with the  $\text{Fe}_{0.50}\text{Mn}_{0.50}\text{O}_x$  catalyst, investigating preparation using  $(\text{NH}_4)_2\text{CO}_3$ ,  $\text{K}_2\text{CO}_3$ ,  $\text{NH}_4\text{OH}$ ,  $\text{KOH}$ , and  $\text{NaOH}$ . In almost all cases, the activity of propane oxidation was increased compared to the  $\text{Na}_2\text{CO}_3$ -prepared catalyst, with the hydroxide-precipitated catalysts generally being more active than the carbonates. The  $\text{NH}_4\text{OH}$  catalyst was the best performing and this was thought to be due to the formation of a highly active mixed defect spinel structure. Results demonstrate that highly active mixed metal oxide total oxidation catalysts can be prepared using abundant elements, and the choice of precipitating agent is important to maximise the activity.

**Keywords:** iron manganese oxide; VOCs; propane; catalytic oxidation



**Citation:** Shah, P.M.; Bailey, L.A.; Morgan, D.J.; Taylor, S.H. The Effect of Metal Ratio and Precipitation Agent on Highly Active Iron-Manganese Mixed Metal Oxide Catalysts for Propane Total Oxidation. *Catalysts* **2023**, *13*, 794. <https://doi.org/10.3390/catal13050794>

Academic Editors: Eduardo Miró, Ezequiel David Banus and Juan Pablo Bortolozzi

Received: 30 March 2023

Revised: 19 April 2023

Accepted: 20 April 2023

Published: 23 April 2023



**Copyright:** © 2023 by the authors. Licensee MDPI, Basel, Switzerland. This article is an open access article distributed under the terms and conditions of the Creative Commons Attribution (CC BY) license (<https://creativecommons.org/licenses/by/4.0/>).

## 1. Introduction

Volatile organic compounds (VOCs) are a form of atmospheric pollutants emitted from both environmental and man-made sources. They are often potent greenhouse gasses with global warming potentials greater than carbon dioxide and contribute to climate change [1]. VOCs have been found to directly damage human health, with aromatic compounds being highly carcinogenic and linked to cases of leukaemia [2]. Atmospheric VOCs also readily react with  $\text{NO}_x$  leading to the formation of low-level ozone and smog [3,4]. This is particularly prevalent in urban environments where the ozone is a large contributor to air pollution, one of the leading causes of preventable death globally [5]. These negative consequences have led to efforts to reduce VOC concentrations in the atmosphere, with regulations introduced to limit emissions. The Gothenburg Protocol and China's 13th five-year plan are all significant legislation that included targets of reducing the release of VOCs [6–8].

A number of methods have been developed with the aim of reducing the emissions of VOCs, with adsorption, absorption, catalytic oxidation, and thermal oxidation all receiving extensive research. Catalytic oxidation is a technology that has received increased interest due to its benefits over other techniques. Unlike thermal oxidation, it is highly selective towards non-toxic products, while also proceeding at a much lower operating temperature [9]. Catalytic oxidation is also a destructive technique, unlike adsorption and absorption, converting the VOC to a more benign compound than simply immobilising it. A further benefit of catalytic oxidation is the ability to treat low concentrations and complex VOC streams containing multiple compounds [10].

Propane total oxidation to  $\text{CO}_2$  and  $\text{H}_2\text{O}$  has received significant research interest in the context of VOC emission control. Propane is highly stable when compared to other VOCs, making it challenging to fully oxidise; this makes it an effective model for determining catalytic performance [11]. Atmospheric concentrations of propane have also risen in recent years due to an increase in the use of liquified petroleum gas (LPG) as a fuel, of which propane is a major constituent [12].

Metal oxide and mixed metal oxide catalysts have seen a recent increase in research into their application as VOC oxidation catalysts, due to the high costs of precursor materials used for preparing supported noble metal catalysts [13]. Manganese oxide catalysts have been identified as particularly active materials for a wide range of VOC oxidation reactions, including propane, hexane, toluene, naphthalene, ethanol, and ethyl acetate [14–36]. The performance has been found to be highly dependent on surface area and manganese oxidation state, making the material-preparation method particularly important [8,23]. Manganese-containing mixed metal oxides have also been studied, with the addition of a second element often making the catalyst more active than the single-metal parent oxides. Ceria-manganese mixed metal oxides have been investigated for a number of VOC oxidation reactions, with manganese-rich materials often found to be the most active [37–40]. Phase segregation of the oxides, manganese oxidation state, and the number of oxygen vacancies are influential over the catalytic activity. Copper-manganese mixed metal oxides have also been evaluated as oxidation catalysts, with the mixed oxides found to be more active than the parent oxides for the oxidation of naphthalene, benzene, and CO [41–44].

Iron is an element with low cost and high abundance, and it exhibits a range of different stable oxides. While metallic iron has been used in large-scale applications such as ammonia synthesis and Fischer–Tropsch reactions [45], there have been limited investigations into iron oxide for its ability to oxidise VOCs. Iron oxides have been tested with mixed success for VOCs including ethanol, propane, toluene, and naphthalene [31,46–48]. Iron has shown more promise as part of a mixed metal oxide with iron-cobalt oxides showing increased performance over cobalt oxide for several oxidation reactions [49–51]. Iron-manganese mixed metal oxides have been investigated as a VOC oxidation catalyst. Solid solutions have been reported to form with the incorporation of iron into the manganese lattice leading to the formation of a greater number of surface defect sites [52,53], which has been used to explain increased performance for the oxidation of toluene, ethanol, and ethyl acetate [46,53].

This work investigates the effect of the Fe:Mn ratio on mixed metal oxide catalyst performance for the total oxidation of propane. Catalysts were initially prepared by co-precipitation with  $\text{Na}_2\text{CO}_3$  as the precipitating agent. Catalysts were characterised using Brunauer–Emmett–Teller (BET) surface area, X-ray diffraction (XRD), temperature programmed reduction (TPR), scanning electron microscopy (SEM), and X-ray photoelectron spectroscopy (XPS). The nature of the precipitating agent was also investigated to study how it affects catalyst characteristics and consequently activity.

## 2. Results and Discussion

### 2.1. Performance of Sodium Carbonate Coprecipitated Catalysts

A range of iron-manganese mixed metal oxide catalysts was synthesised, along with the parent iron and manganese oxides, with differing Fe:Mn ratios and tested for their propane total oxidation activity (Figure 1a). Negligible propane conversion was seen when a blank reactor tube was used (6% at 600 °C), showing that homogeneous gas phase reactions were not responsible for any appreciable activity. All samples showed high selectivity to  $\text{CO}_2$  (>99%) indicating that total oxidation of the propane occurred at all temperatures. The manganese oxide catalyst obtained complete conversion of propane at 500 °C while the  $\text{FeO}_x$  was the least active material tested. As the concentration of iron in the manganese oxide sample increased, the catalytic performance also increased. The activity was at a maximum for  $\text{Fe}_{0.50}\text{Mn}_{0.50}\text{O}_x$ , which produced complete conversion by 350 °C. As the sample then became increasingly manganese-rich, the performance started

to decline. This is demonstrated in Figure 1b which shows the  $T_{50}$  values decrease as iron is added to the manganese oxide until a minimum was reached at 252 °C for the  $\text{Fe}_{0.50}\text{Mn}_{0.50}\text{O}_x$  catalyst. The following trend for catalyst activity was identified:

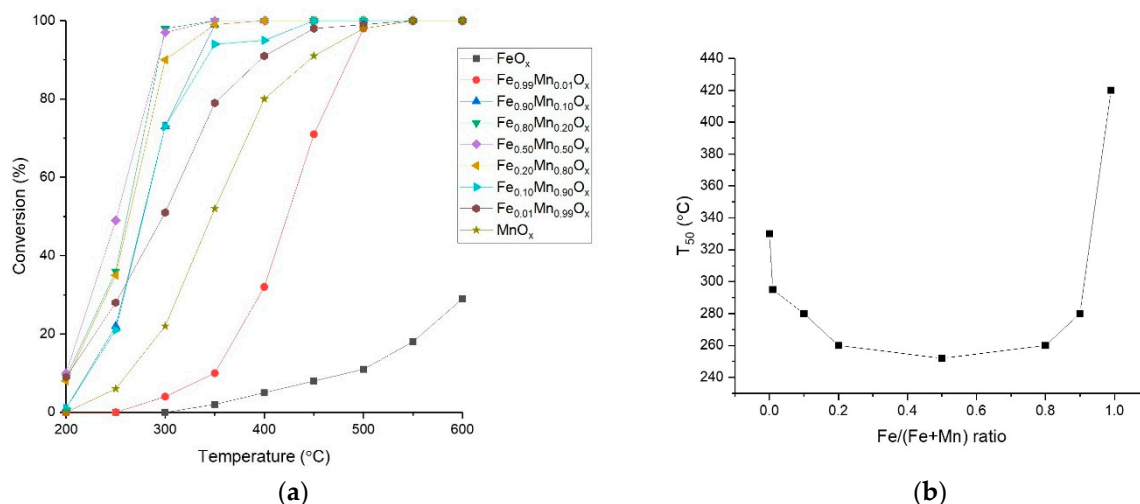
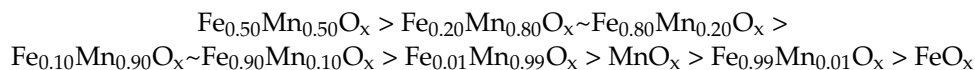


**Figure 1.** (a) Propane conversion as a function of temperature for iron-manganese mixed metal oxide catalysts. (b) Molar ratio Fe/(Fe+Mn) dependence of  $T_{50}$  for propane oxidation. Reaction conditions: 5000 ppm propane in air, Gas Hourly Space Velocity (GHSV) = 45,000  $\text{h}^{-1}$ , Temperature range = 200–600 °C.

The activity data shows that even a small addition of iron to the manganese oxide catalysts led to a large improvement in the activity of propane oxidation. As the base iron oxide sample performed significantly worse than all other catalysts tested, there is a synergy between the two metals, changing the characteristics of the newly formed mixed metal oxide to produce a catalyst considerably more active for propane oxidation. It is also interesting to note that the addition of a small amount of manganese to the iron oxide also significantly promoted activity, indicating the importance of the synergistic combination.

## 2.2. Characterisation of Sodium Carbonate Coprecipitated Catalysts

Powder XRD analysis of the calcined catalysts is presented in Figure 2 and Table 1. The diffraction pattern for the manganese oxide sample suggests a mixture of manganese oxide phases present. Peaks at 29°, 39°, and 57° all indicate  $\text{MnO}_2$  phases, while peaks at 33°, 37°, 44°, and 52° are assigned to  $\text{Mn}_2\text{O}_3$ . The iron oxide had eight major peaks at around 24°, 33°, 35°, 40°, 49°, 54°, 62°, and 64° corresponding to the (012), (104), (110), (113), (024), (116), (214), and (300) lattice planes of  $\text{Fe}_2\text{O}_3$ . It is clear from the diffraction patterns that even a small addition of iron to the manganese oxide led to large changes in the bulk structure of the materials. Additional peaks were now present in the manganese-rich catalysts corresponding to  $\text{Fe}_2\text{O}_3$  suggesting some phase separation of the manganese oxide and iron oxide.  $\text{Fe}_{0.50}\text{Mn}_{0.50}\text{O}_x$  also contained both manganese oxide and iron oxide, as phase separated  $\text{Fe}_2\text{O}_3$  and  $\text{Mn}_2\text{O}_3$ . This can help explain the greater performance of this catalyst as previous research has shown  $\text{Mn}_2\text{O}_3$  to be more active for VOC oxidation than  $\text{MnO}_2$  [30]. As the materials became iron-rich, there were only  $\text{Fe}_2\text{O}_3$  phases present with no peaks arising from manganese oxides. This, along with the slight shift to a higher angle of these peaks, suggests the incorporation of the manganese into the iron oxide lattice.

Information on the crystallite size of both the  $\text{FeO}_x$  and  $\text{MnO}_x$  phases, derived from X-ray line broadening by application of the Scherrer equation, is presented in Table 1. The crystallite size for the manganese oxide decreased when iron was added. For the iron oxide,

the addition of manganese to the system led to a large increase in iron oxide crystallite size. Previous studies into mixed metal oxides have suggested that a decrease in crystallite size is due to the incorporation of one species into the lattice of the other [39,54]. This could be the case for our catalysts, with the iron incorporated into the manganese oxide lattice.

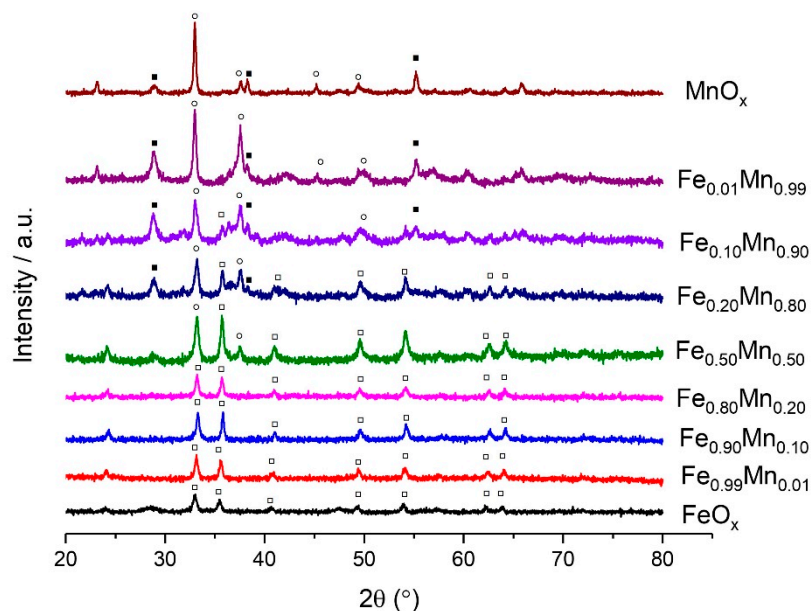


**Figure 2.** Powder XRD patterns of iron-manganese mixed metal oxide catalysts. ■— $\text{MnO}_2$ , ○— $\text{Mn}_2\text{O}_3$ , □— $\text{Fe}_2\text{O}_3$ .

**Table 1.** Physiochemical properties extracted from XRD and Brunauer–Emmett–Teller (BET) surface area of the iron-manganese mixed metal oxide catalysts.

Catalyst	Phases Present	Crystallite Size (Å)		Surface Area ( $\text{m}^2 \text{g}^{-1}$ )
		$\text{Fe}_2\text{O}_3$	$\text{Mn}_2\text{O}_3$	
$\text{FeO}_x$	$\text{Fe}_2\text{O}_3$	190	-	62
$\text{Fe}_{0.99}\text{Mn}_{0.01}\text{O}_x$	$\text{Fe}_2\text{O}_3$	387	-	23
$\text{Fe}_{0.90}\text{Mn}_{0.10}\text{O}_x$	$\text{Fe}_2\text{O}_3$	322	-	25
$\text{Fe}_{0.80}\text{Mn}_{0.20}\text{O}_x$	$\text{Fe}_2\text{O}_3$	280	-	31
$\text{Fe}_{0.50}\text{Mn}_{0.50}\text{O}_x$	$\text{Fe}_2\text{O}_3, \text{Mn}_2\text{O}_3$	291	143	42
$\text{Fe}_{0.20}\text{Mn}_{0.80}\text{O}_x$	$\text{Fe}_2\text{O}_3, \text{MnO}_2, \text{Mn}_2\text{O}_3$	366	188	33
$\text{Fe}_{0.10}\text{Mn}_{0.90}\text{O}_x$	$\text{Fe}_2\text{O}_3, \text{MnO}_2, \text{Mn}_2\text{O}_3$	225	160	31
$\text{Fe}_{0.01}\text{Mn}_{0.99}\text{O}_x$	$\text{MnO}_2, \text{Mn}_2\text{O}_3$	-	317	35
$\text{MnO}_x$	$\text{MnO}_2, \text{Mn}_2\text{O}_3$	-	361	18

The catalyst surface areas were measured using the BET method (Table 1). The manganese oxide had the lowest surface area of the materials studied with iron oxide having the highest. As iron was added to the manganese oxide, there was a large increase in surface area. The manganese-rich samples all have similar surface areas.  $\text{Fe}_{0.50}\text{Mn}_{0.50}\text{O}_x$  has the highest surface area of the mixed metal oxides, while as the samples become more iron-rich, the surface area decreased.

Temperature-programmed reduction profiles (Figure 3) for the manganese oxide catalyst had two peaks at around 310 °C and 410 °C corresponding to the reduction of  $\text{MnO}_2$  to  $\text{Mn}_2\text{O}_3$  and  $\text{Mn}_2\text{O}_3$  to  $\text{MnO}$ , respectively [55]. The iron oxide sample also had two peaks at around 420 °C corresponding to the reduction of  $\text{Fe}_2\text{O}_3$  to  $\text{Fe}_3\text{O}_4$  and a broad peak from around 500 °C to 700 °C assigned to  $\text{Fe}_3\text{O}_4$  to  $\text{FeO}$  [56,57]. The  $\text{Fe}_{0.01}\text{Mn}_{0.99}\text{O}_x$  sample also contained two peaks assigned to the same reduction steps as manganese oxide. The first peak for the  $\text{Fe}_{0.01}\text{Mn}_{0.99}\text{O}_x$  sample was at a lower temperature than

the manganese oxide, suggesting that small amounts of iron lead to easier reducibility.  $\text{Fe}_{0.10}\text{Mn}_{0.90}\text{O}_x$  and  $\text{Fe}_{0.20}\text{Mn}_{0.80}\text{O}_x$  contain four peaks, with the peaks at 300 °C and 420 °C corresponding to manganese oxide, while the peaks at 470 °C and between 600 and 700 °C related to the reduction of iron oxide species. For the  $\text{Fe}_{0.10}\text{Mn}_{0.90}\text{O}_x$  catalyst the 420 °C manganese oxide peak and 470 °C iron oxide peak overlap, giving the appearance of a shoulder. The peaks corresponding to the  $\text{Fe}_2\text{O}_3$  to  $\text{Fe}_3\text{O}_4$  reduction shifted to a higher temperature, suggesting that the iron oxide became more difficult to reduce. The intensity of the iron oxide peaks also increased, reflecting the increased iron content in the material. The  $\text{Fe}_{0.50}\text{Mn}_{0.50}\text{O}_x$  also has four peaks corresponding to the manganese oxide and iron oxide reductions previously assigned. The intensity of the manganese peaks decreased in magnitude, while the iron oxide peaks were larger, again corresponding to the changes in metal concentrations. The iron-rich samples all have a broad peak between 500–700 °C corresponding to the  $\text{Fe}_3\text{O}_4$  to  $\text{FeO}$  reduction. They also have an additional peak at a lower temperature, which could correspond to the  $\text{Fe}_2\text{O}_3$  to  $\text{Fe}_3\text{O}_4$  reduction. There are significant differences in the temperature at which this peak occurred, suggesting large changes in the redox properties of the iron-rich samples. The manganese-rich samples appear to be a combination of reduction profiles of both the parent oxides, while the iron-rich samples appear different to both the manganese oxide and iron oxide. This suggests distinct areas of both manganese oxide and iron oxide present in the manganese-rich catalysts, while manganese was incorporated into the iron lattice for the iron-rich samples, agreeing with the XRD data.

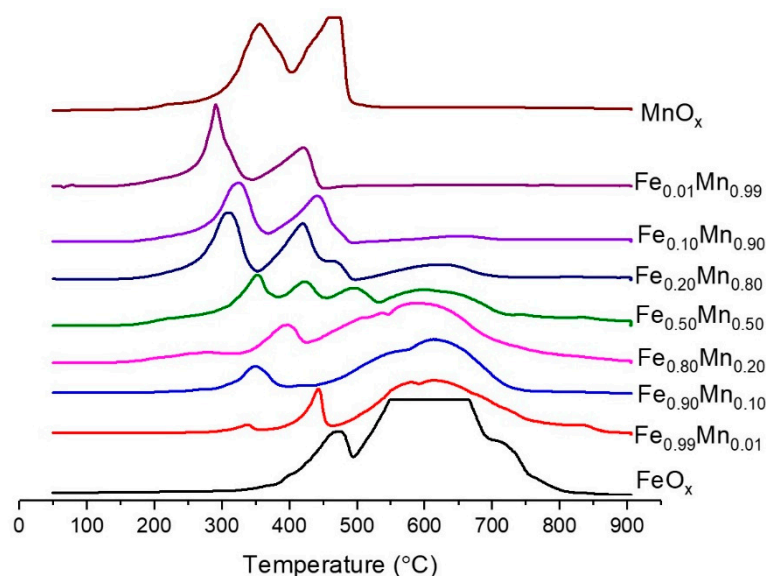


**Figure 3.**  $\text{H}_2$  temperature programmed reduction (TPR) profiles of iron-manganese mixed metal oxide catalysts. Analysis conditions: 30 mL  $\text{min}^{-1}$  10%  $\text{H}_2/\text{Ar}$ , Temperature range 50–800 °C, 10 °C  $\text{min}^{-1}$  ramp rate.

Images of the catalysts were obtained using scanning electron microscopy (Figure S1). Iron oxide forms a spherical sponge-like morphology, which was maintained across the iron-rich samples. This could suggest some level of manganese incorporation as no areas of stacked plate-like morphology indicative of manganese oxide were identified. For the  $\text{Fe}_{0.50}\text{Mn}_{0.50}\text{O}_x$  and manganese-rich samples, the morphology mostly resembled the stacked plate-like structure of manganese oxide. There were areas of spherical sponge-like particles present, suggesting that full incorporation had not occurred, and some phase separation was evident. EDX was run in conjunction with SEM imaging with elemental maps constructed (Figures S2 and S3). These maps show high levels of mixing between the metals suggesting that, for the most part, there was the incorporation of the metals, and the areas of phase separation were not widespread. The EDX also showed very large amounts

of sodium present despite significant washing occurring during the material synthesis. This has been seen in previous studies of mixed metal oxide catalysts and has been shown to have a negative effect on the activity of propane oxidation.

X-ray photoelectron spectroscopy was performed on the samples, with elemental surface concentrations presented in Table 2. There is good agreement between the theoretical Fe:Mn ratios and the relative surface concentrations of each component. The XPS also agrees with the EDX in showing large amounts of sodium present in the catalysts, with surface concentrations being particularly high for iron-rich catalysts.

**Table 2.** Elemental surface concentrations of the iron-manganese mixed metal oxides derived from XPS.

Catalyst	Relative Surface Fe Concentration (%)	Relative Surface Mn Concentration (%)	Surface Na Concentration (Atomic %)
FeO <sub>x</sub>	100	0	3.4
Fe <sub>0.99</sub> Mn <sub>0.01</sub> O <sub>x</sub>	97.9	2.1	12.4
Fe <sub>0.90</sub> Mn <sub>0.10</sub> O <sub>x</sub>	84.8	15.2	7.4
Fe <sub>0.80</sub> Mn <sub>0.20</sub> O <sub>x</sub>	71.2	28.8	10.8
Fe <sub>0.50</sub> Mn <sub>0.50</sub> O <sub>x</sub>	49.6	50.4	4.9
Fe <sub>0.20</sub> Mn <sub>0.80</sub> O <sub>x</sub>	36.0	64.0	1.8
Fe <sub>0.10</sub> Mn <sub>0.90</sub> O <sub>x</sub>	21.1	78.9	1.9
Fe <sub>0.01</sub> Mn <sub>0.99</sub> O <sub>x</sub>	13.5	86.5	1.2
MnO <sub>x</sub>	0	100	6.7

The analysis of the Fe 2p XPS spectra (Figure 4) shows peaks for all iron-containing samples at 710.6 eV and 724.4 eV, characteristic of Fe<sup>3+</sup> containing oxides, and supported by the presence of Fe<sup>3+</sup> specific satellite structure at ca. 719 eV [58,59]. This suggests the presence of Fe<sub>2</sub>O<sub>3</sub>, in agreement with both XRD and TPR analysis. As the iron content decreased, a shift of 0.6 eV towards lower binding energy was noted. We attribute this to increased electron density from the manganese which can act as an electron donor [60].

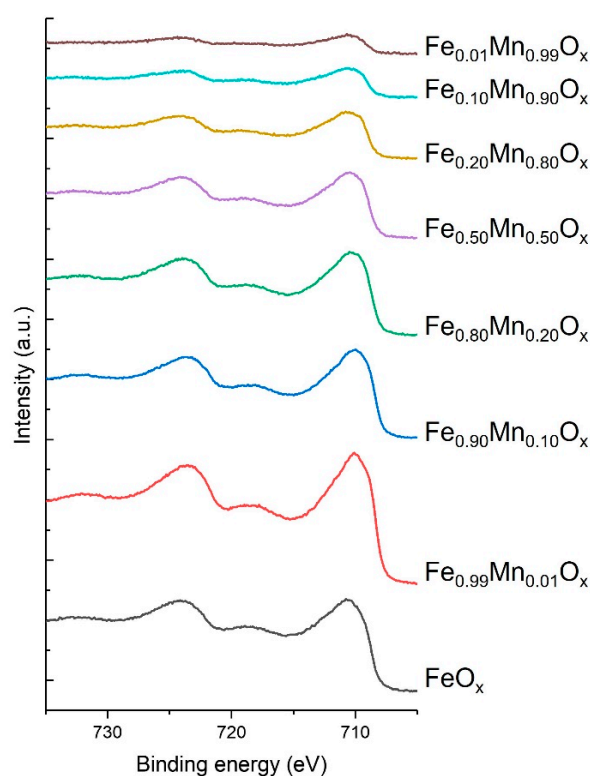


**Figure 4.** Fe 2p XPS spectra for the iron-manganese mixed metal oxide catalysts.

Analysis of Mn spectra can be rather difficult, especially if multiple states are present [61], herein the Mn  $2p_{3/2}$  peak binding energy varies between 641.2 eV (low concentrations) and 641.8 eV (high concentrations of Mn and bulk oxide), and the values are consistent with  $MnO_2$  and  $MnOOH$  [61].

The multiplet splitting of the Mn 3s peak has been used to help elucidate the manganese oxidation state (Figure 5) [62]. Not every manganese-containing catalyst had this feature, due to the concentration of the Mn present and the relative sensitivity of these orbitals to the photoemission process, only where the manganese content was 50% or more could this measurement be reliably made. The splitting values can be seen in Table 3. All samples except the  $Fe_{0.50}Mn_{0.50}O_x$  had a splitting of 5.4 eV or lower, indicative of manganese in a 4+ oxidation state and  $MnO_2$  being present, agreeing with the XRD analysis. However, the Mn 2p spectra (Figure S4) also show an increase in the asymmetry to the lower binding energy side of Mn  $2p_{3/2}$ , suggesting a possible increase in the amount of Mn 3+ present as the Fe content is increased. This is consistent with the magnitude of the 3s splitting increasing with increasing amounts of Fe suggesting the presence of multiple manganese oxidation states, and hence a greater number of defect sites. Increased defect site concentration has been shown to be beneficial for propane oxidation and may explain the activity trends. The splitting of 5.4 eV for the  $Fe_{0.50}Mn_{0.50}O_x$  instead identifies  $Mn_2O_3$  and can help explain why this is the most active catalyst. This is because manganese oxide present as  $Mn_2O_3$  has been found to be more active than  $MnO_2$  for a number of VOC oxidation reactions.

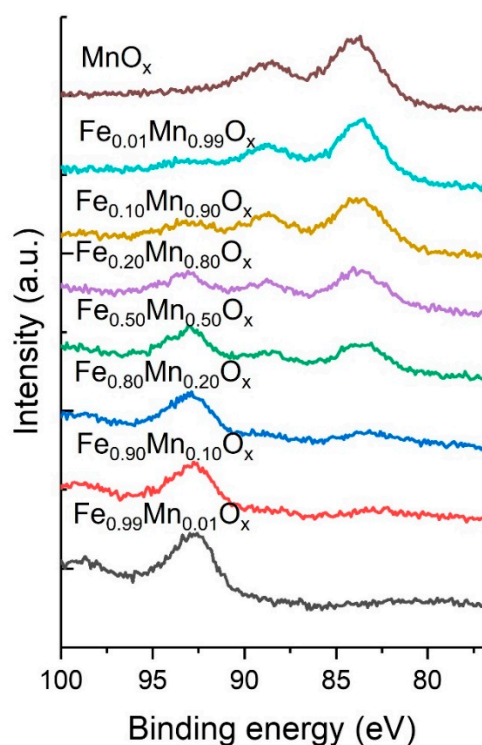


**Figure 5.** Mn 3s XPS spectra for iron-manganese mixed metal oxide catalysts.

With the elemental analysis showing large concentrations of sodium remaining in the catalyst, even after washing, alternative precipitating agents were investigated. Previous work has identified that sodium was an inhibitor for propane total oxidation, so reducing the concentration present or removing it all together should lead to catalysts with greater activity [39]. As the  $Fe_{0.50}Mn_{0.50}O_x$  catalyst was the most active Fe:Mn ratio, it was selected for further investigation. The precipitation agents investigated were potassium carbonate, ammonium carbonate, sodium hydroxide, potassium hydroxide, and ammonium hydroxide.

**Table 3.** Chemical properties of the surface iron and manganese species determined from XPS.

Catalyst	Surface Oxidation State of Fe	Magnitude of Mn 3s Peak Splitting (eV)	Surface Oxidation State of Mn
Fe <sub>0.99</sub> Mn <sub>0.01</sub> O <sub>x</sub>	3+	-	-
Fe <sub>0.90</sub> Mn <sub>0.10</sub> O <sub>x</sub>	3+	-	-
Fe <sub>0.80</sub> Mn <sub>0.20</sub> O <sub>x</sub>	3+	-	-
Fe <sub>0.50</sub> Mn <sub>0.50</sub> O <sub>x</sub>	3+	5.4	3+
Fe <sub>0.20</sub> Mn <sub>0.80</sub> O <sub>x</sub>	3+	5.1	4+
Fe <sub>0.10</sub> Mn <sub>0.90</sub> O <sub>x</sub>	3+	4.9	4+
Fe <sub>0.01</sub> Mn <sub>0.99</sub> O <sub>x</sub>	3+	4.8	4+
MnO <sub>x</sub>	-	4.8	4+

### 2.3. Influence of Precipitation Agent

The activities for propane total oxidation for catalysts with varying precipitating agents are shown in Figure 6. All catalysts showed very high activity and selectivity for CO<sub>2</sub>. All catalysts, except for the K<sub>2</sub>CO<sub>3</sub>-prepared catalyst, had greater performance than the sodium carbonate-prepared catalyst, with close to 100% conversion achieved by 300 °C. The most active catalyst was precipitated using NH<sub>4</sub>OH, having a T<sub>50</sub> of 210 °C, roughly 20 °C lower than the next best catalyst. The choice of anion used as the precipitating agent appears to influence catalyst activity, as all of the hydroxide-derived catalysts were more active for propane oxidation than the equivalent carbonate species. The cation also plays a role in catalyst performance, with the ammonium-based materials being more active than the equivalent sodium ones, which in turn, were more active than the potassium-based catalysts. It is worth noting that the sodium hydroxide-prepared catalyst was the second most active suggesting that sodium-containing precursors should not necessarily be ruled out for producing active catalysts. The performance trends for the catalysts tested are as follows:

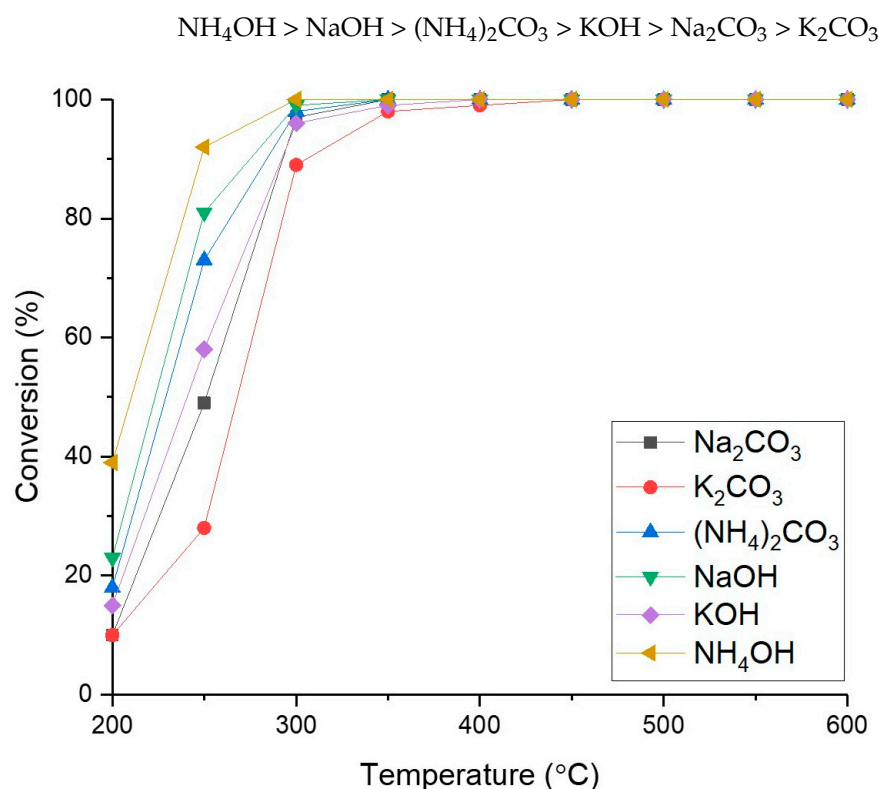


**Figure 6.** Propane conversion as a function of temperature of Fe<sub>0.50</sub>Mn<sub>0.50</sub>O<sub>x</sub> catalysts synthesised using different precipitating agents. Reaction conditions: 5000 ppm propane in air, Gas Hourly Space Velocity (GHSV) = 45,000 h<sup>-1</sup>, Temperature = 200–600 °C.



The catalysts produced here are highly active for propane oxidation. This work aimed to produce high-performing catalysts while using cheaper and more sustainable elements. In previous works, we have investigated the mixed metal oxides of ceria-zirconia and ceria-manganese, allowing direct comparison between these catalysts [39,63]. Figure 7 shows the  $T_{50}$ s of the best-performing catalysts from each study. It is clearly demonstrated that the iron-manganese catalysts are more active than both mixed metal oxide catalysts of ceria-zirconia and ceria-manganese. The  $T_{50}$  of 210 °C is 70 °C lower than that for the best-performing Ce-Mn catalyst, demonstrating the significant impact the addition of iron has on manganese oxide catalysts compared to ceria. The  $T_{50}$  is also 145 °C lower than that of the most active ceria-zirconia catalyst investigated. A further catalyst that is generally considered highly active for propane oxidation is cobalt oxide ( $\text{Co}_3\text{O}_4$ ). Previous works in the literature identified that  $T_{50}$ s were often between 200 °C and 230 °C [64–68], which are comparable to the  $\text{Fe}_{0.50}\text{Mn}_{0.50}\text{O}_x$  catalyst when  $\text{NH}_4\text{OH}$  was used as the precipitating agent. Cobalt is a scarcer resource than both iron and manganese, making the similar performance of the iron-manganese catalyst of great interest [69].

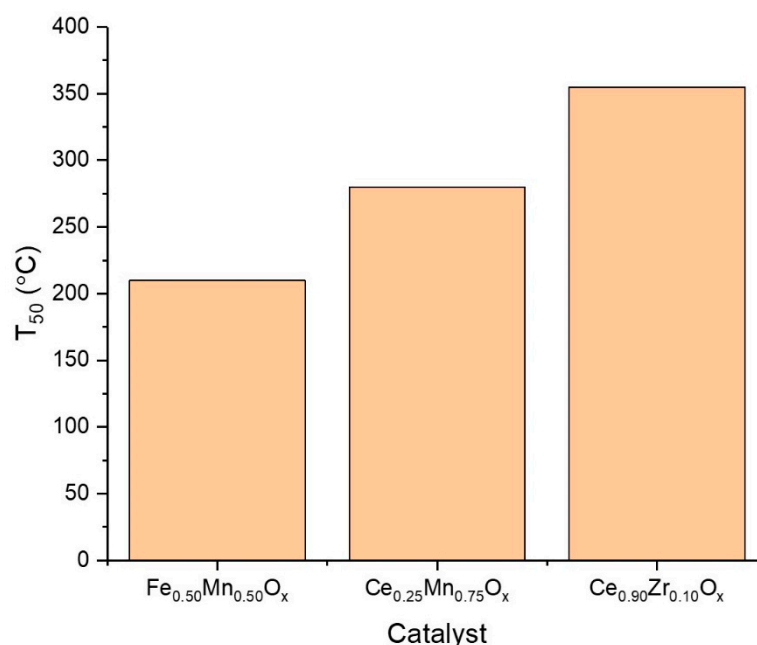


**Figure 7.** Comparison of the  $T_{50}$ s of the most active catalyst  $\text{Fe}_{0.50}\text{Mn}_{0.50}\text{O}_x$  catalyst with other mixed metal oxide catalysts from the literature for the total oxidation of propane. Reaction conditions: 5000 ppm propane in air, Gas Hourly Space Velocity (GHSV) = 45,000  $\text{h}^{-1}$ , Temperature = 200–600 °C.

Powder X-ray diffraction was used to analyse the phases present (Figure 8). The diffraction patterns produced were very similar for the carbonate and hydroxide precursors, respectively. The carbonate catalysts all had peaks at 24°, 33°, 35°, 40°, 49°, and 54°, indicating the presence of  $\text{Fe}_2\text{O}_3$  phases, while the hydroxide precursor materials had peaks at 30°, 36°, 43°, 57°, and 62° suggesting the iron existed as  $\text{Fe}_3\text{O}_4$  and a mixed iron-manganese species ( $\text{FeMnO}_3$ ) [56]. The hydroxide samples were more active than the analogous carbonate sample, suggesting that the species formed are more active for propane oxidation than  $\text{Fe}_2\text{O}_3$ . Work that looked into the supported iron oxide nanoparticles for the deep oxidation of toluene has suggested that  $\text{Fe}_3\text{O}_4$  is more active than  $\text{Fe}_2\text{O}_3$  [70]. However, as not every hydroxide-made catalyst is more active than every carbonate sample, this is not the only factor influencing the performance. Peaks for manganese-containing phases were also present in the diffraction patterns for the  $\text{Na}_2\text{CO}_3$  and  $\text{K}_2\text{CO}_3$  precipitated catalysts, corresponding to  $\text{Mn}_2\text{O}_3$ .

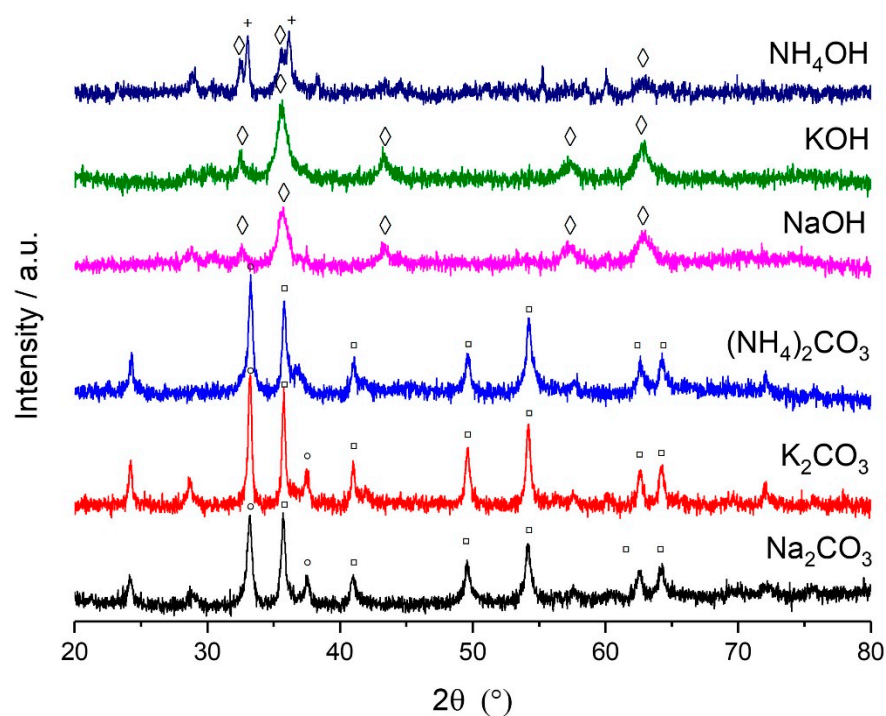


**Figure 8.** Powder X-ray diffraction patterns of  $\text{Fe}_{0.50}\text{Mn}_{0.50}\text{O}_x$  catalysts prepared using different precipitating agents.  $\circ$ — $\text{Mn}_2\text{O}_3$ ,  $\square$ — $\text{Fe}_2\text{O}_3$ ,  $\diamond$ — $\text{Fe}_3\text{O}_4$ ,  $+$ — $\text{FeMnO}_3$ .

Iron oxide crystallite sizes are shown in Table 4. Large differences in the crystallite size were observed depending on whether a hydroxide or carbonate precipitating agent was used. The catalysts made with carbonate had significantly larger crystallites compared to the hydroxides. There is a correlation between crystallite size and activity, the  $\text{K}_2\text{CO}_3$  catalyst, which has the largest crystallite size at 443 Å, is the least active, while the  $\text{NH}_4\text{OH}$  and  $\text{NaOH}$  are the most active and have the smallest crystallite size.

**Table 4.** Physical properties of the  $\text{Fe}_{0.50}\text{Mn}_{0.50}\text{O}_x$  catalysts prepared using different precipitating agents.

Catalyst	$\text{FeO}_x$ Crystallite Size (Å)	$\text{MnO}_x$ Crystallite Size (Å)	BET Surface Area ( $\text{m}^2\text{g}^{-1}$ )
$\text{Na}_2\text{CO}_3$	291	143	42
$\text{K}_2\text{CO}_3$	443	136	49
$(\text{NH}_4)_2\text{CO}_3$	274	-	88
$\text{NaOH}$	88	-	63
$\text{KOH}$	100	-	68
$\text{NH}_4\text{OH}$	91	240	98

Table 4 also shows the BET surface areas for the range of catalysts. Generally, the carbonate-precipitated catalysts had a lower surface area than the analogous hydroxide-precipitated catalyst. For both the carbonate and hydroxide samples there was little difference between the surface areas for the sodium and potassium precipitating agents. The ammonium-based precursors both had much higher surface areas than the other precipitating agents and could be a factor to help explain the greater activity of these catalysts. The increased surface area of the mixed metal oxide catalysts, when compared to the parent oxides, suggests that they do not exist as a simple mixture of the individual component oxides and that a more complex, mixed phase has formed. This has been used as evidence in previous works for the formation of solid solutions or spinel phases [46,71,72].

The reduction profiles show large differences between hydroxide- and carbonate-precipitated catalysts (Figure 9). Catalysts prepared using carbonate precipitating agents had four regions of reduction features. The peaks at around 300 °C and 450 °C correspond to the reduction of manganese species, suggesting the presence of both  $\text{MnO}_2$  and  $\text{Mn}_2\text{O}_3$ . The peaks at around 380 °C and the broad peak between 500–650 °C relate to the reduction of iron oxide, suggesting the presence of  $\text{Fe}_2\text{O}_3$ , confirming results from XRD. There were slight shifts in the temperature of these peaks, suggesting subtle differences in the reducibility of these materials. The peaks relating to manganese reduction for the  $(\text{NH}_4)_2\text{CO}_3$  catalyst are at a lower temperature than for the other carbonate-derived catalysts, indicating easier reducibility of the manganese species. This could help explain the increased catalytic activity for this catalyst, as the lability of oxygen species increased.

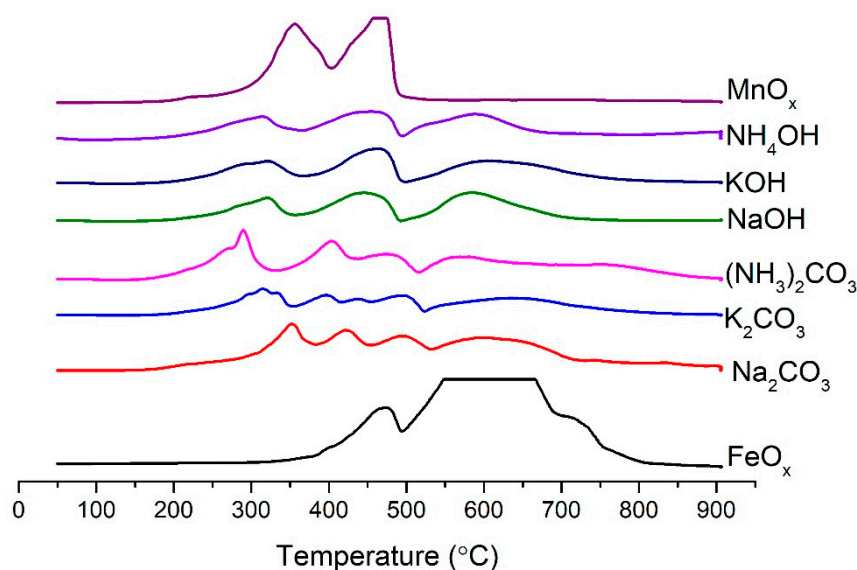


**Figure 9.**  $\text{H}_2$  TPR profiles of the  $\text{Fe}_{0.50}\text{Mn}_{0.50}\text{O}_x$  samples. Analysis conditions:  $30 \text{ mL min}^{-1}$   $10\% \text{ H}_2/\text{Ar}$ , Temperature range  $50\text{--}800 \text{ }^\circ\text{C}$ ,  $10 \text{ }^\circ\text{C min}^{-1}$  ramp rate.

The profiles for the hydroxide catalysts are all very similar, with three peaks at  $310 \text{ }^\circ\text{C}$ ,  $460 \text{ }^\circ\text{C}$ , and  $575 \text{ }^\circ\text{C}$ . These profiles are no longer a combination of the reduction profiles of the parent iron and manganese oxides, suggesting structural changes in the catalysts. The temperature of the peak corresponds well with the formation of a mixed defect spinel structure of  $\text{FeMnO}_3$  [73,74]. The low-temperature peak corresponds to the reduction of  $\text{FeMnO}_3$  to an  $(\text{Fe, Mn})_3\text{O}_4$  mixed spinel phase, with the peak at  $460 \text{ }^\circ\text{C}$  assigned to a further reduction to an iron-manganese mixed phase, manganowustite. The high-temperature peak relates to the reduction of manganowustite to metallic iron. This can help explain the high activity of the hydroxide catalysts as materials with spinel-like structures have often been found to be highly active for VOC oxidation reactions [75–80]. This agrees with the XRD scattering pattern for this material which also suggested the formation of a mixed iron-manganese structure.

SEM images of the catalysts are shown in Figure S5. The choice of precipitating agent does not appear to have a significant impact on catalyst morphology, with a spherical sponge morphology seen throughout. No plate-like structures were identified, suggesting the bulk structure for these samples was similar to iron oxide. EDX analysis (Figure S6) was performed in conjunction with the SEM to provide an understanding of the elemental composition of the catalysts. Sodium was still present for the sodium hydroxide precipitated catalyst, however, in lower concentrations than for  $\text{Na}_2\text{CO}_3$ . This could help explain the improved performance of the hydroxide catalyst, as excessive sodium is detrimental to activity. Elemental maps also show good levels of mixing of the iron and manganese species.

Surface species concentration, determined by XPS, suggests large differences in the amount of potassium and sodium present at the surface between the hydroxide and carbonate precipitated catalysts. Much lower concentrations of both potassium and sodium were found at the surface for the hydroxide catalysts than for the carbonate ones (Table S1). With surface sodium being shown to inhibit propane oxidation for other mixed metal oxides, this could explain improved performance for the hydroxide catalysts. This finding could be extended to the presence of potassium as well.

The Fe 2p XPS spectra (Figure 10) show three peaks for all samples. These three peaks again indicate that Fe is present in a 3+ oxidation state, indicative of the iron oxide existing as Fe<sub>2</sub>O<sub>3</sub>. The width of the peak centred at 710.7 eV exhibits a small degree of asymmetry to the lower binding energy side for the hydroxide-precipitated catalysts than for those prepared using carbonates. Previous studies have suggested that this shows the presence of Fe<sup>2+</sup> alongside Fe<sup>3+</sup> with the iron being in a mixture of oxidation states and agrees with the TPR analysis performed on these samples, which suggested the formation of a mixed spinel structure. Here, iron would be present in both the 2+ and 3+ states.

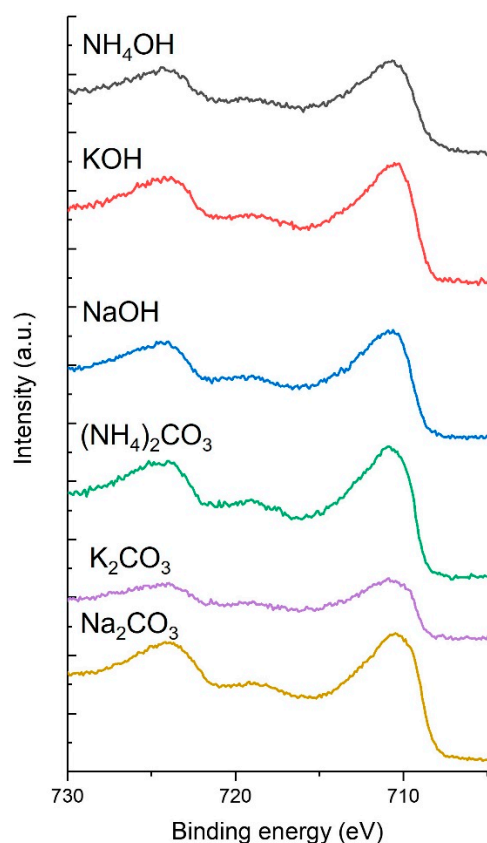


Figure 10. Fe 2p XPS spectra of the Fe<sub>0.50</sub>Mn<sub>0.50</sub>O<sub>x</sub> catalysts.

### 3. Experimental

#### 3.1. Catalyst Preparation

Iron-manganese mixed metal oxides with a range of Fe:Mn ratios were synthesised by co-precipitation using an auto-titration method (Metrohm Titrando, Runcorn, UK). The Fe:Mn ratios studied were 100:0, 99:1, 90:10, 80:20, 50:50, 20:80, 10:90, 1:99, 0:100. Appropriate volumes of Fe(NO<sub>3</sub>)<sub>3</sub> · 9H<sub>2</sub>O (Sigma-Aldrich, Gillingham, UK, 99%, 0.25 M) and Mn(NO<sub>3</sub>)<sub>2</sub> · 4H<sub>2</sub>O (Sigma-Aldrich, Gillingham, UK, 99%, 0.25 M) solutions were pre-mixed and precipitated using Na<sub>2</sub>CO<sub>3</sub> solution (anhydrous, Sigma-Aldrich, Gillingham, UK, 1 M). The pH was kept constant at pH 9 and metal salt solutions were dosed at 3 mL min<sup>-1</sup>. The mixture was left to age at 60 °C for 2 h with the solid recovered by

filtration and washed using 1 L of hot water. The sample was dried at 110 °C for 16 h before calcination under flowing air at 500 °C for 3 h.

Fe<sub>0.50</sub>Mn<sub>0.50</sub>O<sub>x</sub> catalysts were prepared using the method described above, except a range of precipitating agents were used. These were 1 M solutions of K<sub>2</sub>CO<sub>3</sub> (Sigma-Aldrich, Gillingham, UK), (NH<sub>4</sub>)<sub>2</sub>CO<sub>3</sub> (Sigma-Aldrich, Gillingham, UK), NaOH (Sigma-Aldrich, Gillingham, UK), KOH (Sigma-Aldrich, Gillingham, UK), and NH<sub>4</sub>OH (Sigma-Aldrich, Gillingham, UK) used to precipitate the catalyst precursors, which were then recovered, dried, and calcined using the same procedures described above.

### 3.2. Catalyst Testing

The catalyst activity was evaluated using a gas-phase fixed bed microreactor. A constant volume of catalyst sample was fixed between quartz wool plugs in a 6 mm o.d. stainless steel reactor tube which was heated using a tube furnace (Carbolite Gero, Hope Valley, UK). Propane oxidation was investigated using a mixture of 5000 ppm propane in the air using a flow of 50 mL min<sup>-1</sup> giving a gas hourly space velocity of 45,000 h<sup>-1</sup>. Catalyst performance was studied between 200 and 600 °C at 50 °C intervals, with temperature controlled using a K-type thermocouple placed just above the catalyst bed. Gas analysis was performed using gas chromatography (Agilent 7090B, Stockport, UK) fitted with a thermal conductivity detector (TCD) and flame ionization detector (FID). A methanizer was used to monitor concentrations of CO<sub>2</sub>, CO, and propane. The separation of gases was enabled by a Haysep Q (80–100 mesh, 1.8 m × 3.2 mm) and MolSieve 13× (80–100 mesh, 2 m × 3.2 mm) column. The activity was allowed to stabilise at each temperature with analysis repeated until three consistent data sets were obtained, confirming that a steady state was achieved.

### 3.3. Catalyst Characterisation

Powder X-ray diffraction was undertaken using a Panalytical X'Pert diffractometer (Malvern Panalytical, Malvern, UK) using a copper X-ray source operating at 40 kV and 40 mA. Identification of catalyst phases was performed by comparing experimental patterns to the ICDD database.

The surface area analysis was performed using a Quantachrome Quadrasorb Evo Analyser (Quantachrome, Hook, UK). Samples were outgassed under vacuum at 250 °C for 16 h before nitrogen adsorption isotherms at −196 °C were measured. The Braunauer–Emmett–Teller (BET) theory was used to calculate sample surface area.

Temperature programmed reduction (TPR) was conducted on a Quantachrome Chem-BET (Quantachrome, Hook, UK) apparatus. A total of 50 mg of sample was analysed and pre-treated under a flow of helium at 120 °C for an hour, before the reduction profile was obtained using a 10% H<sub>2</sub>/Ar gas flow, increasing the temperature from ambient to 800 °C at 10 °C min<sup>-1</sup>.

Scanning electron microscopy (SEM) and electron dispersive X-ray spectroscopy (EDX) were performed on a Tescan MAIA3 FEG-SEM microscope (Tescan, Cambridge, UK) and Oxford Instruments X-ray Max<sup>N</sup> 80 detector (Oxford Instruments, Abingdon, UK).

X-ray photoelectron spectroscopy (XPS) was conducted on a Thermo Scientific K-Alpha+ spectrometer (Thermo Fisher Scientific, East Grinstead, UK) operating at 72 W using Al K $\alpha$  monochromator. High-resolution and survey scans were performed at pass energies of 40 eV and 150 eV, and step sizes of 0.1 eV and 1 eV, respectively. Spectra were calibrated against the 248.8 eV C (1s) peak. The analysis was performed employing CasaXPS software (v2.3.24) removing the Shirley background and using Schofield sensitivity factors and an energy dependence of −0.6.

## 4. Conclusions

Iron-manganese mixed metal oxide catalysts were prepared using coprecipitation and assessed for the total oxidation of propane. All catalysts investigated were active for this reaction with the Fe<sub>0.50</sub>Mn<sub>0.50</sub>O<sub>x</sub> catalyst being the most active Fe:Mn ratio. This was

assigned to some phase separation between the iron oxide and manganese oxide phases and the presence of  $\text{Mn}_2\text{O}_3$ . All other catalysts contained  $\text{MnO}_2$ , which has previously been found to be less active. The  $\text{Fe}_{0.50}\text{Mn}_{0.50}\text{O}_x$  catalyst also had the highest surface area, and there was a relationship between increasing surface area and activity.

High surface concentrations of sodium, a known catalyst inhibitor, led to investigations into the use of other precipitating agents for catalyst synthesis. The most active  $\text{Fe}_{0.50}\text{Mn}_{0.50}\text{O}_x$  catalyst was prepared by precipitation with  $\text{NH}_4\text{OH}$ . It was exceptionally active for propane oxidation, exhibiting a  $T_{50}$  value of 210 °C, making it comparable in performance to some of the most active catalysts in the literature. Generally, it was found that hydroxide-based precipitating agents produced better-performing catalysts than those made using carbonate. High activity is thought to be due to the formation of a highly active mixed spinel structure.

**Supplementary Materials:** The following supporting information can be downloaded at: <https://www.mdpi.com/article/10.3390/catal13050794/s1>, Figure S1: SEM images of iron-manganese mixed metal oxides prepared by sodium carbonate co-precipitation, Figure S2: SEM-EDX images of base oxides prepared by sodium carbonate co-precipitation, Figure S3: SEM-EDX images of iron-manganese mixed metal oxides prepared by sodium carbonate co-precipitation, Figure S4: Mn 2p XPS spectra for iron-manganese mixed metal oxides prepared by sodium carbonate co-precipitation, Figure S5: SEM images of  $\text{Fe}_{0.50}\text{Mn}_{0.50}\text{O}_x$  mixed metal oxides prepared using different precipitating agents, Figure S6: SEM-EDX images of  $\text{Fe}_{0.50}\text{Mn}_{0.50}\text{O}_x$  mixed metal oxides prepared using different precipitating agents, Table S1: Elemental surface composition of  $\text{Fe}_{0.50}\text{Mn}_{0.50}\text{O}_x$  mixed metal oxides prepared using different precipitating agents derived from XPS.

**Author Contributions:** Conceptualization, S.H.T.; data curation, P.M.S. and D.J.M.; formal analysis, P.M.S., L.A.B. and D.J.M.; investigation, L.A.B. and S.H.T.; supervision, S.H.T.; writing—original draft, L.A.B. and S.H.T.; writing—review and editing, P.M.S., L.A.B., D.J.M. and S.H.T. All authors have read and agreed to the published version of the manuscript.

**Funding:** This research received no external funding.

**Data Availability Statement:** Data is contained within the article and Supplementary Information.

**Conflicts of Interest:** The authors declare no conflict of interest.

## References

1. He, C.; Cheng, J.; Zhang, X.; Douthwaite, M.; Pattison, S.; Hao, Z. Recent Advances in the Catalytic Oxidation of Volatile Organic Compounds: A Review Based on Pollutant Sorts and Sources. *Chem. Rev.* **2019**, *119*, 4471–4568. [CrossRef] [PubMed]
2. Evuti, A. A Synopsis on Biogenic and Anthropogenic Volatile Organic Compounds Emissions: Hazards and Control. *Int. J. Eng. Sci.* **2013**, *2*, 145–153.
3. Duan, J.; Tan, J.; Yang, L.; Wu, S.; Hao, J. Concentration, Sources and Ozone Formation Potential of Volatile Organic Compounds (VOCs) during Ozone Episode in Beijing. *Atmos. Res.* **2008**, *88*, 25–35. [CrossRef]
4. Ryerson, T.B.; Trainer, M.; Holloway, J.S.; Parrish, D.D.; Huey, L.G.; Sueper, D.T.; Frost, G.J.; Donnelly, S.G.; Schauffler, S.; Atlas, E.L.; et al. Observations of Ozone Formation in Power Plant Plumes and Implications for Ozone Control Strategies. *Science* **2001**, *292*, 719–723. [CrossRef]
5. Landrigan, P.J.; Fuller, R.; Acosta, N.J.R.; Adeyi, O.; Arnold, R.; Basu, N.; Baldé, A.B.; Bertollini, R.; Bose-O'Reilly, S.; Boufford, J.I.; et al. The Lancet Commission on Pollution and Health. *Lancet* **2018**, *391*, 462–512. [CrossRef]
6. Scirè, S.; Liotta, L.F. Supported Gold Catalysts for the Total Oxidation of Volatile Organic Compounds. *Appl. Catal. B Environ.* **2012**, *125*, 222–246. [CrossRef]
7. Guo, Y.; Wen, M.; Li, G.; An, T. Recent Advances in VOC Elimination by Catalytic Oxidation Technology onto Various Nanoparticles Catalysts: A Critical Review. *Appl. Catal. B Environ.* **2021**, *281*, 119447. [CrossRef]
8. Kamal, M.S.; Razzak, S.A.; Hossain, M.M. Catalytic Oxidation of Volatile Organic Compounds (VOCs)—A Review. *Atmos. Environ.* **2016**, *140*, 117–134. [CrossRef]
9. Krishnamurthy, A.; Adebayo, B.; Gelles, T.; Rownaghi, A.; Rezaei, F. Abatement of Gaseous Volatile Organic Compounds: A Process Perspective. *Catal. Today* **2020**, *350*, 100–119. [CrossRef]
10. Taylor, M.N.; Zhou, W.; Garcia, T.; Solsona, B.; Carley, A.F.; Kiely, C.J.; Taylor, S.H. Synergy between Tungsten and Palladium Supported on Titania for the Catalytic Total Oxidation of Propane. *J. Catal.* **2012**, *285*, 103–114. [CrossRef]
11. Tichenor, B.A.; Palazzolo, M.A. Destruction of Volatile Organic Compounds via Catalytic Incineration. *Environ. Prog.* **1987**, *6*, 172–176. [CrossRef]

12. Enterkin, J.A.; Setthapun, W.; Elam, J.W.; Christensen, S.T.; Rabuffetti, F.A.; Marks, L.D.; Stair, P.C.; Poeppelmeier, K.R.; Marshall, C.L. Propane Oxidation over Pt/SrTiO<sub>3</sub> Nanocuboids. *ACS Catal.* **2011**, *1*, 629–635. [[CrossRef](#)]
13. Aggett, K.; Davies, T.E.; Morgan, D.J.; Hewes, D.; Taylor, S.H. The Influence of Precursor on the Preparation of CeO<sub>2</sub> Catalysts for the Total Oxidation of the Volatile Organic Compound Propane. *Catalysts* **2021**, *11*, 1461. [[CrossRef](#)]
14. Bratan, V.; Vasile, A.; Chesler, P.; Hornoiu, C. Insights into the Redox and Structural Properties of CoOx and MnOx: Fundamental Factors Affecting the Catalytic Performance in the Oxidation Process of VOCs. *Catalysts* **2022**, *12*, 1134. [[CrossRef](#)]
15. Huang, N.; Qu, Z.; Dong, C.; Qin, Y.; Duan, X. Superior Performance of  $\alpha$ @ $\beta$ -MnO<sub>2</sub> for the Toluene Oxidation: Active Interface and Oxygen Vacancy. *Appl. Catal. A Gen.* **2018**, *560*, 195–205. [[CrossRef](#)]
16. Zhang, X.; Zhao, H.; Song, Z.; Liu, W.; Zhao, J.; Ma, Z.; Zhao, M.; Xing, Y. Insight into the Effect of Oxygen Species and Mn Chemical Valence over MnOx on the Catalytic Oxidation of Toluene. *Appl. Surf. Sci.* **2019**, *493*, 9–17. [[CrossRef](#)]
17. Everaert, K.; Baeyens, J. Catalytic Combustion of Volatile Organic Compounds. *J. Hazard. Mater.* **2004**, *109*, 113–139. [[CrossRef](#)]
18. Puértolas, B.; Smith, A.; Vázquez, I.; Dejoz, A.; Moragues, A.; Garcia, T.; Solsona, B. The Different Catalytic Behaviour in the Propane Total Oxidation of Cobalt and Manganese Oxides Prepared by a Wet Combustion Procedure. *Chem. Eng. J.* **2013**, *229*, 547–558. [[CrossRef](#)]
19. Xie, Y.; Yu, Y.; Gong, X.; Guo, Y.; Wang, Y.; Lu, G. Effect of the Crystal Plane Figure on the Catalytic Performance of MnO<sub>2</sub> for the Total Oxidation of Propane. *CrystEngComm* **2015**, *17*, 3005–3014. [[CrossRef](#)]
20. Castaño, M.H.; Molina, R.; Moreno, S. Catalytic Oxidation of VOCs on MnMgAlOx Mixed Oxides Obtained by Auto-Combustion. *J. Mol. Catal. A Chem.* **2015**, *398*, 358–367. [[CrossRef](#)]
21. Finocchio, E.; Busca, G. Characterization and Hydrocarbon Oxidation Activity of Coprecipitated Mixed Oxides Mn<sub>3</sub>O<sub>4</sub>/Al<sub>2</sub>O<sub>3</sub>. *Catal. Today* **2001**, *70*, 213–225. [[CrossRef](#)]
22. Baldi, M.; Finocchio, E.; Milella, F.; Busca, G. Catalytic Combustion of C<sub>3</sub> Hydrocarbons and Oxygenates over Mn<sub>3</sub>O<sub>4</sub>. *Appl. Catal. B Environ.* **1998**, *16*, 43–51. [[CrossRef](#)]
23. Lahousse, C.; Bernier, A.; Grange, P.; Delmon, B.; Papaefthimiou, P.; Ioannides, T.; Verykios, X. Evaluation of  $\gamma$ -MnO<sub>2</sub> as a VOC Removal Catalyst: Comparison with a Noble Metal Catalyst. *J. Catal.* **1998**, *178*, 214–225. [[CrossRef](#)]
24. Li, J.; Li, L.; Cheng, W.; Wu, F.; Lu, X.; Li, Z. Controlled Synthesis of Diverse Manganese Oxide-Based Catalysts for Complete Oxidation of Toluene and Carbon Monoxide. *Chem. Eng. J.* **2014**, *244*, 59–67. [[CrossRef](#)]
25. Li, J.; Li, L.; Wu, F.; Zhang, L.; Liu, X. Dispersion–Precipitation Synthesis of Nanorod Mn<sub>3</sub>O<sub>4</sub> with High Reducibility and the Catalytic Complete Oxidation of Air Pollutants. *Catal. Commun.* **2013**, *31*, 52–56. [[CrossRef](#)]
26. Zhang, J.; Li, Y.; Wang, L.; Zhang, C.; He, H. Catalytic Oxidation of Formaldehyde over Manganese Oxides with Different Crystal Structures. *Catal. Sci. Technol.* **2015**, *5*, 2305–2313. [[CrossRef](#)]
27. Rong, S.; Zhang, P.; Liu, F.; Yang, Y. Engineering Crystal Facet of  $\alpha$ -MnO<sub>2</sub> Nanowire for Highly Efficient Catalytic Oxidation of Carcinogenic Airborne Formaldehyde. *ACS Catal.* **2018**, *8*, 3435–3446. [[CrossRef](#)]
28. Wang, J.; Li, J.; Jiang, C.; Zhou, P.; Zhang, P.; Yu, J. The Effect of Manganese Vacancy in Birnessite-Type MnO<sub>2</sub> on Room-Temperature Oxidation of Formaldehyde in Air. *Appl. Catal. B Environ.* **2017**, *204*, 147–155. [[CrossRef](#)]
29. Bai, B.; Li, J.; Hao, J. 1D-MnO<sub>2</sub>, 2D-MnO<sub>2</sub> and 3D-MnO<sub>2</sub> for Low-Temperature Oxidation of Ethanol. *Appl. Catal. B Environ.* **2015**, *164*, 241–250. [[CrossRef](#)]
30. Garcia, T.; Sellick, D.; Varela, F.; Vázquez, I.; Dejoz, A.; Agouram, S.; Taylor, S.H.; Solsona, B. Total Oxidation of Naphthalene Using Bulk Manganese Oxide Catalysts. *Appl. Catal. A Gen.* **2013**, *450*, 169–177. [[CrossRef](#)]
31. García, T.; Solsona, B.; Taylor, S.H. Naphthalene Total Oxidation over Metal Oxide Catalysts. *Appl. Catal. B Environ.* **2006**, *66*, 92–99. [[CrossRef](#)]
32. Pérez, H.; Navarro, P.; Torres, G.; Sanz, O.; Montes, M. Evaluation of Manganese OMS-like Cryptomelane Supported on SBA-15 in the Oxidation of Ethyl Acetate. *Catal. Today* **2013**, *212*, 149–156. [[CrossRef](#)]
33. Pérez, H.; Navarro, P.; Delgado, J.J.; Montes, M. Mn-SBA15 Catalysts Prepared by Impregnation: Influence of the Manganese Precursor. *Appl. Catal. A Gen.* **2011**, *400*, 238–248. [[CrossRef](#)]
34. Chen, L.; Liu, Y.; Fang, X.; Cheng, Y. Simple Strategy for the Construction of Oxygen Vacancies on  $\alpha$ -MnO<sub>2</sub> Catalyst to Improve Toluene Catalytic Oxidation. *J. Hazard. Mater.* **2021**, *409*, 125020. [[CrossRef](#)] [[PubMed](#)]
35. Zhang, X.; Lv, X.; Bi, F.; Lu, G.; Wang, Y. Highly Efficient Mn<sub>2</sub>O<sub>3</sub> Catalysts Derived from Mn-MOFs for Toluene Oxidation: The Influence of MOFs Precursors. *Mol. Catal.* **2020**, *482*, 110701. [[CrossRef](#)]
36. Lyu, Y.; Li, C.; Du, X.; Zhu, Y.; Zhang, Y.; Li, S. Catalytic Oxidation of Toluene over MnO<sub>2</sub> Catalysts with Different Mn (II) Precursors and the Study of Reaction Pathway. *Fuel* **2020**, *262*, 116610. [[CrossRef](#)]
37. Li, H.; Qi, G.; Tana, Z.; Zhang, X.; Huang, X.; Li, W.; Shen, W. Low-Temperature Oxidation of Ethanol over a Mn<sub>0.6</sub>Ce<sub>0.4</sub>O<sub>2</sub> Mixed Oxide. *Appl. Catal. B Environ.* **2011**, *103*, 54–61. [[CrossRef](#)]
38. Chen, J.; Chen, X.; Chen, X.; Xu, W.; Xu, Z.; Jia, H.; Chen, J. Homogeneous Introduction of CeO<sub>y</sub> into MnOx-Based Catalyst for Oxidation of Aromatic VOCs. *Appl. Catal. B Environ.* **2018**, *224*, 825–835. [[CrossRef](#)]
39. Shah, P.M.; Bailey, L.A.; Taylor, S.H. The Influence of Cerium to Manganese Ratio and Preparation Method on the Activity of Ceria-Manganese Mixed Metal Oxide Catalysts for VOC Total Oxidation. *Catalysts* **2023**, *13*, 114. [[CrossRef](#)]
40. Matějová, L.; Topka, P.; Jiráťová, K.; Šolcová, O. Total Oxidation of Model Volatile Organic Compounds over Some Commercial Catalysts. *Appl. Catal. A Gen.* **2012**, *443–444*, 40–49. [[CrossRef](#)]

41. Clarke, T.J.; Kondrat, S.A.; Taylor, S.H. Total Oxidation of Naphthalene Using Copper Manganese Oxide Catalysts. *Catal. Today* **2015**, *258*, 610–615. [[CrossRef](#)]
42. Cao, H.; Li, X.; Chen, Y.; Gong, M.; Wang, J. Effect of Loading Content of Copper Oxides on Performance of Mn-Cu Mixed Oxide Catalysts for Catalytic Combustion of Benzene. *J. Rare Earths* **2012**, *30*, 871–877. [[CrossRef](#)]
43. Tang, W.; Wu, X.; Li, S.; Shan, X.; Liu, G.; Chen, Y. Co-Nanocasting Synthesis of Mesoporous Cu–Mn Composite Oxides and Their Promoted Catalytic Activities for Gaseous Benzene Removal. *Appl. Catal. B Environ.* **2015**, *162*, 110–121. [[CrossRef](#)]
44. Clarke, T.J.; Davies, T.E.; Kondrat, S.A.; Taylor, S.H. Mechanochemical Synthesis of Copper Manganese Oxide for the Ambient Temperature Oxidation of Carbon Monoxide. *Appl. Catal. B Environ.* **2015**, *165*, 222–231. [[CrossRef](#)]
45. Oliveira, L.C.A.; Fabris, J.D.; Pereira, M.C. Iron Oxides and Their Applications in Catalytic Processes: A Review. *Quím. Nova* **2013**, *36*, 123–130. [[CrossRef](#)]
46. Morales, M.R.; Barbero, B.P.; Cadús, L.E. Combustion of Volatile Organic Compounds on Manganese Iron or Nickel Mixed Oxide Catalysts. *Appl. Catal. B Environ.* **2007**, *74*, 1–10. [[CrossRef](#)]
47. Solsona, B.; García, T.; Sanchis, R.; Soriano, M.D.; Moreno, M.; Rodríguez-Castellón, E.; Agouram, S.; Dejoz, A.; López Nieto, J.M. Total Oxidation of VOCs on Mesoporous Iron Oxide Catalysts: Soft Chemistry Route versus Hard Template Method. *Chem. Eng. J.* **2016**, *290*, 273–281. [[CrossRef](#)]
48. Solsona, B.E.; Garcia, T.; Jones, C.; Taylor, S.H.; Carley, A.F.; Hutchings, G.J. Supported Gold Catalysts for the Total Oxidation of Alkanes and Carbon Monoxide. *Appl. Catal. A Gen.* **2006**, *312*, 67–76. [[CrossRef](#)]
49. Manova, E.; Tsoncheva, T.; Estournès, C.I.; Paneva, D.; Tenchev, K.; Mitov, I.; Petrov, L. Nanosized Iron and Iron–Cobalt Spinel Oxides as Catalysts for Methanol Decomposition. *Appl. Catal. A Gen.* **2006**, *300*, 170–180. [[CrossRef](#)]
50. Hammiche-Bellal, Y.; Zouaoui-Mahzoul, N.; Lounas, I.; Benadda, A.; Benrabaa, R.; Auroux, A.; Meddour-Boukhobza, L.; Djadoun, A. Cobalt and Cobalt-Iron Spinel Oxides as Bulk and Silica Supported Catalysts in the Ethanol Combustion Reaction. *J. Mol. Catal. A Chem.* **2017**, *426*, 97–106. [[CrossRef](#)]
51. Biabani-Ravandi, A.; Rezaei, M.; Fattah, Z. Study of Fe–Co Mixed Metal Oxide Nanoparticles in the Catalytic Low-Temperature CO Oxidation. *Process Saf. Environ. Prot.* **2013**, *91*, 489–494. [[CrossRef](#)]
52. Kedesdy, H.H.; Tauber, A. Formation of Manganese Ferrite by Solid-State Reaction. *J. Am. Ceram. Soc.* **1956**, *39*, 425–431. [[CrossRef](#)]
53. Durán, F.G.; Barbero, B.P.; Cadús, L.E.; Rojas, C.; Centeno, M.A.; Odriozola, J.A. Manganese and Iron Oxides as Combustion Catalysts of Volatile Organic Compounds. *Appl. Catal. B Environ.* **2009**, *92*, 194–201. [[CrossRef](#)]
54. Qi, G.; Li, W. NO Oxidation to NO<sub>2</sub> over Manganese-Cerium Mixed Oxides. *Catal. Today* **2015**, *258*, 205–213. [[CrossRef](#)]
55. Stobbe, E.R.; de Boer, B.A.; Geus, J.W. The Reduction and Oxidation Behaviour of Manganese Oxides. *Catal. Today* **1999**, *47*, 161–167. [[CrossRef](#)]
56. Wei, X.; Zhou, Y.; Li, Y.; Shen, W. Polymorphous Transformation of Rod-Shaped Iron Oxides and Their Catalytic Properties in Selective Reduction of NO by NH<sub>3</sub>. *RSC Adv.* **2015**, *5*, 66141–66146. [[CrossRef](#)]
57. Liang, M.; Kang, W.; Xie, K. Comparison of Reduction Behavior of Fe<sub>2</sub>O<sub>3</sub>, ZnO and ZnFe<sub>2</sub>O<sub>4</sub> by TPR Technique. *J. Nat. Gas Chem.* **2009**, *18*, 110–113. [[CrossRef](#)]
58. Grosvenor, A.P.; Kobe, B.A.; Biesinger, M.C.; McIntyre, N.S. Investigation of Multiplet Splitting of Fe 2p XPS Spectra and Bonding in Iron Compounds. *Surf. Interface Anal.* **2004**, *36*, 1564–1574. [[CrossRef](#)]
59. Yamashita, T.; Hayes, P. Analysis of XPS Spectra of Fe<sup>2+</sup> and Fe<sup>3+</sup> Ions in Oxide Materials. *Appl. Surf. Sci.* **2008**, *254*, 2441–2449. [[CrossRef](#)]
60. Liu, Y.; Chen, J.-F.; Zhang, Y. The Effect of Pore Size or Iron Particle Size on the Formation of Light Olefins in Fischer–Tropsch Synthesis. *RSC Adv.* **2015**, *5*, 29002–29007. [[CrossRef](#)]
61. Biesinger, M.C.; Payne, B.P.; Grosvenor, A.P.; Lau, L.W.M.; Gerson, A.R.; Smart, R.S.C. Resolving Surface Chemical States in XPS Analysis of First Row Transition Metals, Oxides and Hydroxides: Cr, Mn, Fe, Co and Ni. *Appl. Surf. Sci.* **2011**, *257*, 2717–2730. [[CrossRef](#)]
62. Junta, J.L.; Hochella, M.F. Manganese (II) Oxidation at Mineral Surfaces: A Microscopic and Spectroscopic Study. *Geochim. Cosmochim. Acta* **1994**, *58*, 4985–4999. [[CrossRef](#)]
63. Shah, P.M.; Day, A.N.; Davies, T.E.; Morgan, D.J.; Taylor, S.H. Mechanochemical Preparation of Ceria-Zirconia Catalysts for the Total Oxidation of Propane and Naphthalene Volatile Organic Compounds. *Appl. Catal. B Environ.* **2019**, *253*, 331–340. [[CrossRef](#)]
64. Solsona, B.; Davies, T.E.; Garcia, T.; Vázquez, I.; Dejoz, A.; Taylor, S.H. Total Oxidation of Propane Using Nanocrystalline Cobalt Oxide and Supported Cobalt Oxide Catalysts. *Appl. Catal. B Environ.* **2008**, *84*, 176–184. [[CrossRef](#)]
65. Garcia, T.; Agouram, S.; Sánchez-Royo, J.F.; Murillo, R.; Mastral, A.M.; Aranda, A.; Vázquez, I.; Dejoz, A.; Solsona, B. Deep Oxidation of Volatile Organic Compounds Using Ordered Cobalt Oxides Prepared by a Nanocasting Route. *Appl. Catal. A Gen.* **2010**, *386*, 16–27. [[CrossRef](#)]
66. Solsona, B.; García, T.; Hutchings, G.J.; Taylor, S.H.; Makkee, M. TAP Reactor Study of the Deep Oxidation of Propane Using Cobalt Oxide and Gold-Containing Cobalt Oxide Catalysts. *Appl. Catal. A Gen.* **2009**, *365*, 222–230. [[CrossRef](#)]
67. Solsona, B.; Vázquez, I.; Garcia, T.; Davies, T.E.; Taylor, S.H. Complete Oxidation of Short Chain Alkanes Using a Nanocrystalline Cobalt Oxide Catalyst. *Catal. Lett.* **2007**, *116*, 116–121. [[CrossRef](#)]



68. Marin, R.P.; Kondrat, S.A.; Pinnell, R.K.; Davies, T.E.; Golunski, S.; Bartley, J.K.; Hutchings, G.J.; Taylor, S.H. Green Preparation of Transition Metal Oxide Catalysts Using Supercritical CO<sub>2</sub> Anti-Solvent Precipitation for the Total Oxidation of Propane. *Appl. Catal. B Environ.* **2013**, *140–141*, 671–679. [[CrossRef](#)]
69. Henckens, M.L.C.M.; Driessen, P.P.J.; Worrell, E. Metal Scarcity and Sustainability, Analyzing the Necessity to Reduce the Extraction of Scarce Metals. *Resour. Conserv. Recycl.* **2014**, *93*, 1–8. [[CrossRef](#)]
70. Trendafilova, I.; Ojeda, M.; Andresen, J.M.; Ristić, A.; Dimitrov, M.; Tušar, N.N.; Atanasova, G.; Popova, M. Low-Temperature Toluene Oxidation on Fe-Containing Modified SBA-15 Materials. *Molecules* **2023**, *28*, 204. [[CrossRef](#)]
71. Venkataswamy, P.; Rao, K.N.; Jampaiah, D.; Reddy, B.M. Nanostructured Manganese Doped Ceria Solid Solutions for CO Oxidation at Lower Temperatures. *Appl. Catal. B Environ.* **2015**, *162*, 122–132. [[CrossRef](#)]
72. Cimino, S.; Lisi, L.; De Rossi, S.; Faticanti, M.; Porta, P. Methane Combustion and CO Oxidation on LaAl<sub>1-x</sub>Mn<sub>x</sub>O<sub>3</sub> Perovskite-Type Oxide Solid Solutions. *Appl. Catal. B Environ.* **2003**, *43*, 397–406. [[CrossRef](#)]
73. Leith, I.R.; Howden, M.G. Temperature-Programmed Reduction of Mixed Iron—Manganese Oxide Catalysts in Hydrogen and Carbon Monoxide. *Appl. Catal.* **1988**, *37*, 75–92. [[CrossRef](#)]
74. Zhang, J.; Fang, K.; Zhang, K.; Li, W.; Sun, Y. Carbon Dispersed Iron-Manganese Catalyst for Light Olefin Synthesis from CO Hydrogenation. *Korean J. Chem. Eng.* **2009**, *26*, 890–894. [[CrossRef](#)]
75. Łojewska, J.; Kołodziej, A.; Dynarowicz-Łątka, P.; Wesełucha-Birczyńska, A. Engineering and Chemical Aspects of the Preparation of Microstructured Cobalt Catalyst for VOC Combustion. *Catal. Today* **2005**, *101*, 81–91. [[CrossRef](#)]
76. Łojewska, J.; Kołodziej, A.; Łojewski, T.; Kapica, R.; Tyczkowski, J. Structured Cobalt Oxide Catalyst for VOC Combustion. Part I: Catalytic and Engineering Correlations. *Appl. Catal. A Gen.* **2009**, *366*, 206–211. [[CrossRef](#)]
77. Łojewska, J.; Kołodziej, A.; Łojewski, T.; Kapica, R.; Tyczkowski, J. Cobalt Catalyst Deposited on Metallic Microstructures for VOC Combustion: Preparation by Non-Equilibrium Plasma. *Catal. Commun.* **2008**, *10*, 142–145. [[CrossRef](#)]
78. Wang, Y.; Jia, A.-P.; Luo, M.-F.; Lu, J.-Q. Highly Active Spinel Type CoCr<sub>2</sub>O<sub>4</sub> Catalysts for Dichloromethane Oxidation. *Appl. Catal. B Environ.* **2015**, *165*, 477–486. [[CrossRef](#)]
79. Zhu, W.; Chen, X.; Li, C.; Liu, Z.; Liang, C. Manipulating Morphology and Surface Engineering of Spinel Cobalt Oxides to Attain High Catalytic Performance for Propane Oxidation. *J. Catal.* **2021**, *396*, 179–191. [[CrossRef](#)]
80. Zhang, S.; Liu, S.; Zhu, X.; Yang, Y.; Hu, W.; Zhao, H.; Qu, R.; Zheng, C.; Gao, X. Low Temperature Catalytic Oxidation of Propane over Cobalt-Cerium Spinel Oxides Catalysts. *Appl. Surf. Sci.* **2019**, *479*, 1132–1140. [[CrossRef](#)]

**Disclaimer/Publisher’s Note:** The statements, opinions and data contained in all publications are solely those of the individual author(s) and contributor(s) and not of MDPI and/or the editor(s). MDPI and/or the editor(s) disclaim responsibility for any injury to people or property resulting from any ideas, methods, instructions or products referred to in the content.